Journal of Computational Physics 344 (2017) 320–338

Contents lists available at ScienceDirect

Journal of Computational Physics

www.elsevier.com/locate/jcp

Physics-based hybrid method for multiscale transport in porous media

Mehrdad Yousefzadeh, Ilenia Battiato [*]

Energy Resources Engineering Department, Stanford University, Stanford, CA 94305, USA

ARTICLE INFO

Article history:
Received 26 September 2016
Received in revised form 20 April 2017
Accepted 21 April 2017
Available online 27 April 2017

Keywords:
Multiscale coupling
Flow and reactive transport in porous media

ABSTRACT

Despite advancements in the development of multiscale models for flow and reactive transport in porous media, the accurate, efficient and physics-based coupling of multiple scales in hybrid models remains a major theoretical and computational challenge. Improving the predictivity of macroscale predictions by means of multiscale algorithms relative to classical *at-scale* models is the primary motivation for the development of multiscale simulators. Yet, very few are the quantitative studies that explicitly address the predictive capability of multiscale coupling algorithms as it is still generally not possible to have *a priori* estimates of the errors that are present when complex flow processes are modeled. We develop a nonintrusive pore-/continuum-scale hybrid model whose coupling error is bounded by the upscaling error, i.e. we build a *predictive* tightly coupled multiscale scheme. This is accomplished by slightly enlarging the subdomain where continuum-scale equations are locally invalid and analytically defining physics-based coupling conditions at the interfaces separating the two computational sub-domains, while enforcing state variable and flux continuity. The proposed multiscale coupling approach retains the advantages of domain decomposition approaches, including the use of existing solvers for each subdomain, while it gains flexibility in the choice of the numerical discretization method and maintains the coupling errors bounded by the upscaling error. We implement the coupling in finite volumes and test the proposed method by modeling flow and transport through a reactive channel and past an array of heterogeneously reactive cylinders.

1. Introduction

Virtually any engineering, environmental and biological system exhibits multiscale features. Porous media, whose geometric and/or chemical heterogeneity is the primary culprit for the onset of multiscale dynamics, are one such example. We focus on the study of flow and reactive transport in porous materials since it is relevant to a rich and diverse set of applications, including battery electrodes and fuel cells [1–4], micro- and ultra-porous coatings [5,6], natural rocks and soils, vegetation [7–9], biological tissues [10] and filtration membranes [11], just to mention a few. Different mathematical and modeling approaches have been introduced to describe at-scale processes ranging from the pore- to the system-scale. Yet, the macroscopic behavior of the system often significantly deviates from mean field approximations: this is due to (i) strong coupling between processes occurring at different scales and (ii) localized invalidation of the macroscale approximation

---

[*] Corresponding author.
E-mail address: ibattiat@stanford.edu (I. Battiato).

http://dx.doi.org/10.1016/j.jcp.2017.04.055

[12–14]. Some examples include cracks propagation in rocks, battery operation at high C-rates [2,15], propagation of highly reacting fronts in porous environments [13,14], membranes clogging [16], abrupt permeability changes in natural rocks and negatively correlated porosity–permeability fields [17,18], etc.

A variety of multiscale methods have been proposed that couple, loosely or tightly, models at different scales (e.g. the pore and the continuum-scale). They generally follow two separate approaches [19]. Monolithic, or intrusive, approaches build a single discrete multiscale operator through which the coupling between scales is ensured. Their advantage lies in robustness, accuracy and stability properties to the detriment of ease in code development. In domain decomposition, or nonintrusive, approaches two or more *at-scale* operators, i.e. operators at distinct individual scales, are coupled through multiscale boundary conditions which allow the communication of processes at different scales to occur without an actual overlap between computational domains. The main advantage of the latter framework lies in the ability to use legacy or existing codes (and solvers) for the development of each of the components of the multiscale system, while their integration is achieved solely through the appropriate formulation of boundary conditions.

A number of multiscale models of flow and reactive transport in porous media have been proposed throughout the years (e.g., [20–25]). The study of noise propagation in hybrid solvers was pioneered by [26] and investigated in subsequent works [27,19,28]. Among domain decomposition approaches, the mesh-free Lagrangian SPH method has been used to couple reactive–diffusive transport in porous media at the pore and continuum-scales [20]. Yet, generalization to advective–diffusive–reactive transport is an open challenge. Mortars methods, first introduced to couple (single-scale) multiphysics systems [29–31], have been successfully implemented to include multi-scale physics [32]. Balhoff et al. [21] developed pore-network mortar domain decomposition approaches to couple pore- and continuum-scale flow. The approach was generalized to model multiscale advective–reactive transport [22] and later extended to include diffusion and dispersion [33]. Despite their ease in implementation, Eulerian pore-networks models (PNMs) typically assume perfect mixing within individual pores. This may not be a justifiable assumption at high Peclét and Damköhler numbers. *Ad hoc* techniques have been proposed to account for pore-scale lack of mixing in PNMs [34]. Tang et al. [35] used mortar methods in the context of finite differences to couple pore- and continuum-scales for biofilm growth due to diffusion and multicomponent reactions in porous media. A review on multiscale models with a focus on mortar coupling methods in the context of PNMs is provided in [36].

Intrusive approaches are characterized by an overlapping domain (or handshake region) where models at different scales are solved. Battiato et al. [23] developed an iterative intrusive method for coupling transport through a fracture with reactive walls. Similarly, Roubinet and Tartakovsky [24] build an overlapping algorithm and replaced the iterative coupling with a semi-analytical coupling technique. Multiscale finite volume approaches and their modifications have been proposed to model coupled-non-linear problems in multiphase flow and transport [37–39]. Reducing the degree of coupling from tight to loose can significantly simplify the treatment of the information passage across scales and increase the computational speed up [40]. A recent review on multiscale methods developed in the context of flow and transport in porous media is given by [41].

Notwithstanding the advancement and success in the numerical development of multiscale models for single and multiphase flow and transport in porous media, the accurate, efficient and physics-based coupling in hybrid models remains a major theoretical and computational challenge. Improving the predictivity of macroscale predictions by means of multiscale algorithms relative to classical *at-scale* models is the primary motivation for the development of multiscale simulators. Yet, very few are the quantitative studies that explicitly address the predictive capability of multiscale coupling algorithms and it is generally not possible to have a priori estimates of the errors that are present when complex flow processes are modeled using coarse or multiscale models constructed via simplified settings or purely numerical coupling schemes. Here, we define a multiscale model predictive if the coupling error is bounded by the theoretical upscaling error. For flow and reactive transport in porous media, the latter is controlled by the order of magnitude of relevant dimensionless numbers, i.e. Damköhler and Peclét numbers [12–14].

In this study, we build a *predictive* nonintrusive pore-/continuum-scale tightly coupled multiscale scheme. This is accomplished by slightly enlarging the domain where the continuum-scale equations are locally invalidated and the pore-scale equations must be solved instead by a volume of the order of the Representative Elementary Volume (the support of the averaging operation). Also, we define appropriate coupling conditions at the interfaces separating the two computational sub-domains, while the enforcing state variable and flux continuity. Simulations in separate sub-domain can be performed using proper solvers for each sub-domain without their customization. The manuscript is organized as follows. In Section 2 we present the pore- and continuum-scale equations for reactive transport in porous media as well as the derivation of the coupling conditions and the hybrid algorithm. In Sections 3 and 4, we apply the proposed method to model flow and transport through a reactive channel and an array of reactive cylinders, respectively. We conclude in Section 5 with a summary of our results.

2. Model formulation

2.1. Pore-scale equations

We consider flow and reactive transport of a solute in a fully-saturated porous medium Ω. Within the pore sub-domain Ω_p, single-phase incompressible flow at low Reynolds numbers is described by the Stokes and continuity equations

$$\mu\nabla^2\mathbf{v} - \nabla p = 0, \quad \nabla\cdot\mathbf{v} = 0, \tag{1}$$

where $\mathbf{v}(\mathbf{x})$, $p(\mathbf{x})$ and μ are the pore-scale velocity, dynamic pressure and fluid dynamic viscosity. Equations (1) are subject to the no-slip boundary condition at the liquid–solid interfaces, $\Gamma_{s\ell}$,

$$\mathbf{v} = \mathbf{0}, \quad \mathbf{x} \in \Gamma_{s\ell}. \tag{2}$$

The mass transport of a solute undergoing a linear heterogeneous reaction on the solid grains can be described by an advection–diffusion equation,

$$\partial_t c + \nabla \cdot (\mathbf{v}c) = D\nabla^2 c, \tag{3}$$

subject to appropriate boundary condition on the solid–liquid interface

$$-\mathbf{n} \cdot D\nabla c = \mathcal{K}c, \quad \mathbf{x} \in \Gamma_{s\ell}, \tag{4}$$

where $c(\mathbf{x}, t)$ is the molar concentration $\left[\mathrm{M\,L^{-3}}\right]$ of the dissolved species, D is the molecular diffusion coefficient, $\mathcal{K}$ is the reaction constant for the surface reaction and $\mathbf{n}$ is the unit normal vector to $\Gamma_{s\ell}$.

2.2. Continuum scale equations

Pore-scale mass transport, as outlined in §2.1, can be described on a multiplicity of scales. For any pore-scale quantity ψ, we may form its volume average as

$$\overline{\psi} = \frac{1}{\phi|\mathcal{V}|} \int_{\mathcal{V}} \psi(\mathbf{y}, t)\mathrm{d}\mathbf{y}, \tag{5}$$

where ϕ is the porosity of the medium, and $\mathcal{V}$ is the averaging volume. Spatial averaging of the flow equations (1) leads to Darcy's law for flow in a continuum porous domain,

$$\overline{\mathbf{v}} = -\frac{\mathbf{k}}{\mu}\nabla\overline{p}, \tag{6}$$

where $\mathbf{k}$ is the permeability of the porous medium, $\overline{\mathbf{v}}$ is Darcy's flux and $\overline{p}$ is the macroscopic pressure. Similarly, pore-scale reactive transport described by (3) and (4) can be homogenized to an effective advection–reaction–dispersion equation (ADRE)

$$\phi\partial_t\overline{c} + \phi\nabla \cdot (\overline{\mathbf{v}}\,\overline{c}) = \nabla \cdot (\mathbf{D}^\star\nabla\overline{c}) - K\overline{c}, \tag{7}$$

where $\mathbf{D}^\star$ is the dispersion tensor and K is the effective reaction rate (e.g., [13,14,2]).

The validity of macroscale equations (6)–(7) is controlled by the subpore-scale heterogeneity of state variables: for example, pore-scale mass transport limitations due to strong advection and/or reactions invalidate the main underlying assumptions of most single-scale continuum models [42,12,2]. This is typical, e.g., in battery systems under high charge/discharge rates [2,15] or strong electrode phase polydispersity [43] and transport of highly reactive species [13,14]. Under such circumstances, single-scale macroscopic models should be replaced by their pore-scale counterparts in those portions of the computational domain where the former are invalidated [26,20,44,23,24,27,41]. Such an approach, often referred to as hybrid or algorithm refinement method, has the advantage of preserving model predictability while maintaining computational costs under control.

The efficient coupling of processes at different scales still represents a major challenge in hybrid multiscale schemes [42]. In the following, we present a novel physics-based coupling approach between continuum- (macroscopic) and pore-scale equations to describe reactive transport in porous media.

2.3. Derivation of a general non-intrusive hybrid formulation

We are concerned with transport regimes in which the validity of (7) breaks down within a sub-domain Ω_p of Ω, with boundary $\partial\Omega_p$. We define Γ to be the locus of the centers of the averaging volumes $\mathcal{V}(\mathbf{x})$, whose envelope is $\partial\Omega_p$, as shown in Fig. 1. We denote $\overline{\Omega}_p$ the domain bounded by Γ. It is worth emphasizing that both macroscopic and pore-scale descriptions are *simultaneously valid* in $\mathcal{V}(\mathbf{x})$ and accordingly on Γ ($\mathbf{x} \in \Gamma$), i.e. the system is perfectly mixed on Γ by construction. Importantly, the choice of $\mathcal{V}(\mathbf{x})$ is arbitrary. The only two conditions $\mathcal{V}(\mathbf{x})$ must satisfy are that (i) it is larger or equal than an REV, and (ii) its boundary $\Gamma(\mathbf{x})$ does not intersect the solid grains of the porous medium where the pore-scale concentration is not defined.

Let $\overline{c}^+(\mathbf{x})$ denote the limiting value of $\overline{c}(\mathbf{x}^+)$ as $\mathbf{x}^+ \to \mathbf{x} \in \Gamma$ from the exterior of $\overline{\Omega}_p$, i.e. $\overline{c}^+(\mathbf{x}) := \lim_{\mathbf{x}^+\to\mathbf{x}} \overline{c}(\mathbf{x}^+)$, and $\overline{c}^- = \overline{c}(\mathbf{x}^-)$ as $\mathbf{x}^- \to \mathbf{x} \in \Gamma$ from the interior of $\overline{\Omega}_p$, i.e. $\overline{c}^-(\mathbf{x}) := \lim_{\mathbf{x}^-\to\mathbf{x}} \overline{c}(\mathbf{x}^-)$. Also, let $\mathcal{V}^{\mathrm{in}}(\mathbf{x}) := \mathcal{V}(\mathbf{x}) \cap \overline{\Omega}_p$ and $\mathcal{V}^{\mathrm{out}}(\mathbf{x}) := \mathcal{V}(\mathbf{x}) \setminus \overline{\Omega}_p$ to form a partition of $\mathcal{V}(\mathbf{x})$ where pore-scale and continuum scale equations are explicitly solved, respectively.

Since the average concentration $\overline{c}$ is continuous everywhere in Ω, it is also continuous across Γ, i.e.

$$\overline{c}^+ = \overline{c}^- \quad \text{for} \quad |\mathbf{x}^+ - \mathbf{x}^-| \to 0. \tag{8}$$

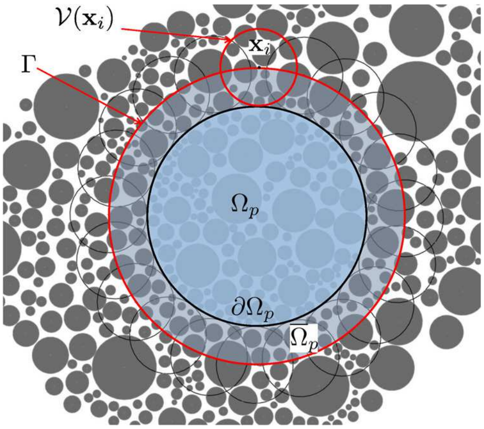

Fig. 1. A schematic representation of the pore-scale and continuum scale domains. Continuum-scale model breaks down in Ω_p which is illustrated in gray. The boundary Γ, locus of the centers of the averaging volumes $\mathcal{V}(\mathbf{x})$ whose envelope is $\partial\Omega_p$.

Using the definition (5), while accounting for the partitions $\mathcal{V}^{\mathrm{out}}$ and $\mathcal{V}^{\mathrm{in}}$, equation (8) can be written as

$$\bar{c}^+ = \frac{1}{\phi|\mathcal{V}|}\int\limits_{\mathcal{V}^{\mathrm{in}}(\mathbf{x}^-)} c(\mathbf{y})\mathrm{d}\mathbf{y} + \frac{1}{\phi|\mathcal{V}|}\int\limits_{\mathcal{V}^{\mathrm{out}}(\mathbf{x}^-)} c(\mathbf{y})\mathrm{d}\mathbf{y}, \quad |\mathbf{x}^+ - \mathbf{x}^-| \to 0, \tag{9}$$

which provides the first coupling condition between the macroscale and microscale quantities $\bar{c}^+$ and c on the boundary Γ. It is worth noticing that the second integral in (9) cannot be explicitly determined as pore-scale concentration is not available in $\mathcal{V}^{\mathrm{out}}$. Since a continuum model is valid on Γ, we can expand $c(\mathbf{y})$ into a Taylor series around the centroid of $\mathcal{V}^{\mathrm{out}}$ and retain the first two terms, i.e.

$$\int\limits_{\mathcal{V}^{\mathrm{out}}(\mathbf{x}^-)} c(\mathbf{y})\mathrm{d}\mathbf{y} = \int\limits_{\mathcal{V}^{\mathrm{out}}(\mathbf{x}^-)} \left[c(\mathbf{x}^-) + \partial_{\mathbf{y}}c(\mathbf{x}^-)(\mathbf{y}-\mathbf{x}^-) + \frac{1}{2}\partial_{\mathbf{yy}}c(\mathbf{x}^-)(\mathbf{y}-\mathbf{x}^-)^2 + \cdots\right]\mathrm{d}\mathbf{y}, \tag{10}$$

where $c(\mathbf{x}^-)$, $\partial_{\mathbf{y}}c(\mathbf{x}^-)$, etc., are constant. Then, (10) can be written as

$$\begin{aligned} & c(\mathbf{x}^-)\int\limits_{\mathcal{V}^{\mathrm{out}}} \mathrm{d}\mathbf{y} + \partial_{\mathbf{y}}c(\mathbf{x}^-)\int\limits_{\mathcal{V}^{\mathrm{out}}}(\mathbf{y}-\mathbf{x}^-)\mathrm{d}\mathbf{y} + \mathcal{O}\left[(\mathbf{y}-\mathbf{x}^-)^2\right] \\ & = c(\mathbf{x}^-)|\mathcal{V}^{\mathrm{out}}(\mathbf{x}^-)| + \partial_{\mathbf{y}}c(\mathbf{x}^-)\left[\int\limits_{\mathcal{V}^{\mathrm{out}}}\mathbf{y}\mathrm{d}\mathbf{y} - \mathbf{x}^-|\mathcal{V}^{\mathrm{out}}(\mathbf{x}^-)|\right] + \mathcal{O}\left[(\mathbf{y}-\mathbf{x}^-)^2\right]. \end{aligned} \tag{11}$$

Using the definition of centroid, $\mathbf{x}^- = |\mathcal{V}^{\mathrm{out}(\mathbf{x}^-)|^{-1}} \int_{\mathcal{V}^{\mathrm{out}}}\mathbf{y}\mathrm{d}\mathbf{y}$, the second term in the previous expansion vanishes and (11) simplifies to

$$\int\limits_{\mathcal{V}^{\mathrm{out}}(\mathbf{x}^-)} c(\mathbf{y})\mathrm{d}\mathbf{y} \approx |\mathcal{V}^{\mathrm{out}}(\mathbf{x}^-)|c(\mathbf{x}^-) + \mathcal{O}\left[(\mathbf{y}-\mathbf{x}^-)^2\right], \tag{12}$$

i.e. the approximation error of (12) is of order $\mathcal{O}(\epsilon^2)$ since $(\mathbf{y}-\mathbf{x}^-) \sim \epsilon$. Inserting (12) into (9), we obtain

$$\bar{c}^+ = \frac{1}{\phi|\mathcal{V}|}\int\limits_{\mathcal{V}^{\mathrm{in}}(\mathbf{x}^-)} c(\mathbf{y})\mathrm{d}\mathbf{y} + \frac{|\mathcal{V}^{\mathrm{out}}(\mathbf{x}^-)|c(\mathbf{x}^-)}{\phi|\mathcal{V}|}. \tag{13}$$

In the coupling boundary condition (13), the right hand side contains only pore scale values and the left hand side consists only of continuum scale values. Another boundary condition is needed to close the system of equations. Continuity of fluxes across Γ requires (see Appendix for details)

$$\mathbf{n}\cdot\phi\overline{(-D\nabla c + \mathbf{v}c)}^- = \mathbf{n}\cdot(-\mathbf{D}^\star\nabla\bar{c}^+ + \phi\overline{\mathbf{v}c}^+). \tag{14}$$

The average on the left hand side of (14) is defined as

$$\mathbf{n}\cdot\phi\overline{(-D\nabla c + \mathbf{v}c)}^- = \mathbf{n}\cdot\left[\frac{\phi}{\phi|\mathcal{V}(\mathbf{x}^-)|}\int\limits_{\mathcal{V}(\mathbf{x}^-)}[-D\nabla c(\mathbf{y},t) + \mathbf{v}(\mathbf{y},t)c(\mathbf{y},t)]\mathrm{d}\mathbf{y}\right], \tag{15}$$

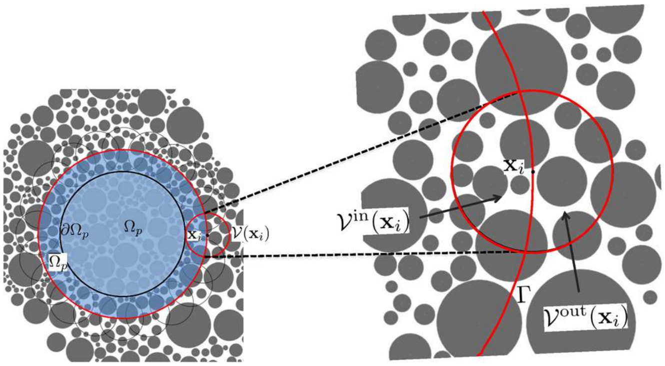

Fig. 2. A schematic representation of an averaging volume and the averaging procedure across the boundary Γ. Pore-scale model is fully resolved on the left of Γ while on the right only a continuum-scale model is applied.

or, in terms of the partitioning domains $\mathcal{V}^{\text{out}}$ and $\mathcal{V}^{\text{in}}$,

$$\mathbf{n}\cdot\phi\overline{(-D\nabla c+\mathbf{v}c)}^{-}=\mathbf{n}\cdot\left[\frac{1}{|\mathcal{V}(\mathbf{x}^{-})|}\int\limits_{\mathcal{V}^{\text{in}}(\mathbf{x}^{-})}[-D\nabla c+\mathbf{v}c]\mathrm{d}\mathbf{y}\right]+q_n, \tag{16}$$

where

$$q_n(\mathbf{x}^{-}):=\frac{1}{|\mathcal{V}|}\mathbf{n}\cdot\int\limits_{\mathcal{V}^{\text{out}}(\mathbf{x}^{-})}[-D\nabla c+\mathbf{v}c]\mathrm{d}\mathbf{y}, \tag{17}$$

is an unknown unresolved flux through the boundary. Expanding the pore-scale velocity and concentration fields around the centroid and retaining the first term, one obtains

$$q_n(\mathbf{x}^{-})\approx\alpha^{-1}\mathbf{n}\cdot[-D\nabla c(\mathbf{x}^{-})+\mathbf{v}(\mathbf{x}^{-})c(\mathbf{x}^{-})], \tag{18}$$

where $\alpha=|\mathcal{V}|/|\mathcal{V}^{\text{out}}|$ and q_n can be approximated as a constant flux over a macroscopic gridblock. We emphasize this approximation is justified since the coupling boundary Γ falls in a well-mixed region by construction. Inserting (16) in (14) yields to the second coupling boundary condition at the interface between the pore-scale and continuum-scale sub-domains

$$\mathbf{n}\cdot(\phi\overline{\mathbf{v}}\overline{c}^{+}-\mathbf{D}^{\star}\nabla\overline{c}^{+})=\frac{1}{|\mathcal{V}|}\mathbf{n}\cdot\int\limits_{\mathcal{V}^{\text{in}}(\mathbf{x}^{-})}(-D\nabla c+\mathbf{v}c)\mathrm{d}y+q_n. \tag{19}$$

The two coupling conditions (13) and (19) will introduce new sources of error, here referred to as coupling error, e.g., (13) introduces a coupling error of order $\mathcal{O}=(\epsilon^2)$. Yet, if the coupling error is bounded by, or of the same order of, the upscaling error then the hybrid model predictivity will not be affected. These assumptions may introduce significant source of error in presence of high concentration gradients along/across the coupling boundary itself, Γ. It is worth noticing, though, that this scenario is excluded by placing the coupling boundary 'away enough' from the reacting front to guarantee that well-mixed conditions are achieved at the coupling location. This is guaranteed by the methodology proposed to define Γ itself, as shown in Fig. 1. Additional sources of error originate from the numerical discretization itself. When ϵ decreases and the error bounds become stricter, the primary source of error is the numerical truncation error. In this scenario, higher order schemes should be employed to implement the coupling. The final form of the coupled system of equations for the hybrid system is

$$\partial_t c+\nabla\cdot(\mathbf{v}c)=D\nabla^2 c,\quad \mathbf{x}\in\overline{\Omega}_p, \tag{20a}$$

$$-\mathbf{n}\cdot D\nabla c=\mathcal{K}c,\quad \mathbf{x}\in\Gamma_{s\ell}, \tag{20b}$$

$$\mathbf{n}\cdot(-D\nabla c+\mathbf{v}c)=\alpha q_n,\quad \mathbf{x}\in\Gamma, \tag{20c}$$

$$\phi\partial_t\overline{c}+\phi\nabla\cdot(\overline{\mathbf{v}}\overline{c})=\nabla\cdot(\mathbf{D}^{\star}\nabla\overline{c})-K^{\star}\overline{c},\quad \mathbf{x}\in\Omega\setminus\overline{\Omega}_p, \tag{20d}$$

$$\mathbf{n}\cdot(\phi\overline{\mathbf{v}}\overline{c}^{+}-\mathbf{D}^{\star}\nabla\overline{c}^{+})=j(c,\mathbf{x})+q_n,\quad \mathbf{x}\in\Gamma, \tag{20e}$$

$$\overline{c}^{+}=i(c,\mathbf{x})+\frac{c(\mathbf{x}^{-})}{\alpha\phi},\quad \mathbf{x}\in\Gamma, \tag{20f}$$

where

$$j(c,\mathbf{x}) := \frac{1}{|\mathcal{V}|} \int\limits_{\mathcal{V}^{\text{in}}(\mathbf{x}^-)} \mathbf{n}\cdot(-D\nabla c + \mathbf{v}c)\mathrm{d}\mathbf{y}, \tag{21a}$$

$$i(c,\mathbf{x}) := \frac{1}{\phi|\mathcal{V}|} \int\limits_{\mathcal{V}^{\text{in}}(\mathbf{x}^-)} c(\mathbf{y})\mathrm{d}\mathbf{y}. \tag{21b}$$

Equations (20)–(21) fully describe the concentration distribution in the pore-space domain $\overline{\Omega}_p$; the continuum-scale equation (20d) is solved in $\Omega \setminus \overline{\Omega}_p$ subject to the boundary condition (20e); finally, continuity of state variables is guaranteed across Γ by (20f).

2.4. Time stepping and algorithm coupling

The system (20) is to be solved iteratively for the unknowns $\bar{c}(\mathbf{x})$, $c(\mathbf{y};\mathbf{x})$ and q_n. We define $G(q_n, c^-)$ and $F(q_n, c^-)$ as

$$G(q_n, c^-) = \bar{c}^+ - i(c,\mathbf{x}) - \frac{|\mathcal{V}^{\text{out}}|}{\phi|\mathcal{V}|}c^-, \tag{22a}$$

$$F(q_n, c^-) = \mathbf{n}\cdot(\phi V\bar{c}^+ - \mathbf{D}^\star\nabla\bar{c}^+) - j(c,\mathbf{x}) - q_n. \tag{22b}$$

The algorithm consists of minimizing the value of the functions F and G. Its steps can be summarized as follows,

1. *Initialization.* At timestep T^N, $c(t = T^N)$ and $\bar{c}(t = T^N)$ are known.
2. *Flux guess.* Make a guess for q_n. This imposes the Robin condition (20c) for the pore-scale equation (20a) at the interface Γ. (The initial guess for q_n is its value at the previous time step.)
3. *Pore-scale equation evolution.* The pore scale equation (20a), supplemented with boundary conditions (20b) and (20c), is evolved from T^N to T^{N+1}.
4. *Evaluation of boundary integrals.* The integral term $j(c,\mathbf{x})$ and $i(c,\mathbf{x})$ in (20e) and (20f), respectively, are evaluated.
5. *Continuum-scale evolution.* The continuum-scale concentration $\bar{c}$ is evolved T^N to T^{N+1} by means of (20d) subject to the boundary condition (20e).
6. *Convergence check.* For a given tolerance ϵ, refine the initial guess of q_n if $|G(q_n, c_\Gamma)| > \epsilon$. This is accomplished by a zero-finding algorithm, i.e. a Newton or quasi-Newton method, for example Broyden's method.

A flowchart of the algorithm is provided in Fig. 3. In the following section, we numerically implement the proposed coupling algorithm. To test the accuracy of the proposed hybrid scheme as well as its computational speed-up compared to full pore-scale simulations, we consider two test cases: flow and transport in a semi-infinite reactive channel (§3) and around an array of impermeable reactive cylinders (§4).

3. Transport in a channel

We consider a fully-developed Stokes flow between two parallel plates a distance L apart. A solute, carried by the fluid, undergoes advection, diffusion and a first-order heterogeneous reaction with the channel walls. The flow domain $\Omega = \{(x, y) : x \in (0,\infty), y \in (0, L)\}$ is bounded by $\partial\Omega = \{(x, y) : x \in (0,\infty), y = 0 \text{ or } L\}$. Under fully-developed flow conditions, pore-scale velocity $\mathbf{v} = [u(y) \quad 0]$ satisfying (1) subject to (2) on $\partial\Omega$ is the Poiseuille flow,

$$u(y) = 4u_m\left[\frac{y}{L} - \left(\frac{y}{L}\right)^2\right], \tag{23}$$

where u_m is the maximum velocity at the center of the fracture. The pore-scale solute concentration $c(x, y)$ satisfies

$$\partial_t c + u(y)\partial_x c = D(\partial^2_{xx}c + \partial^2_{yy}c) \tag{24}$$

subject to

$$-\mathbf{n}\cdot D\nabla c = \mathcal{K}c, \quad y = \{0, L\}, \tag{25}$$

or $D\partial_y c = kc$ for $y = 0$ and $-D\partial_y c = kc$ for $y = L$. The Darcy-scale ADRE equation governing the evolution of the average concentration $\bar{c}(x,t) := L^{-1}\int_0^L c(x, y, t)\mathrm{d}y$ has the form [45]

$$\partial_t\bar{c} + U\partial_x\bar{c} = D^\star\partial^2_{xx}\bar{c} - K^\star\bar{c}, \tag{26}$$

where

$$U = u_m\left(\frac{2}{3} + \frac{4\mathrm{Da}_y}{45}\right), \; K^\star = \frac{\mathcal{K}}{H}\left(1 - \frac{\mathrm{Da}_y}{3}\right), \; D^\star = D\left(1 + \frac{8\mathrm{Pe}_y^2}{945}\right), \tag{27}$$

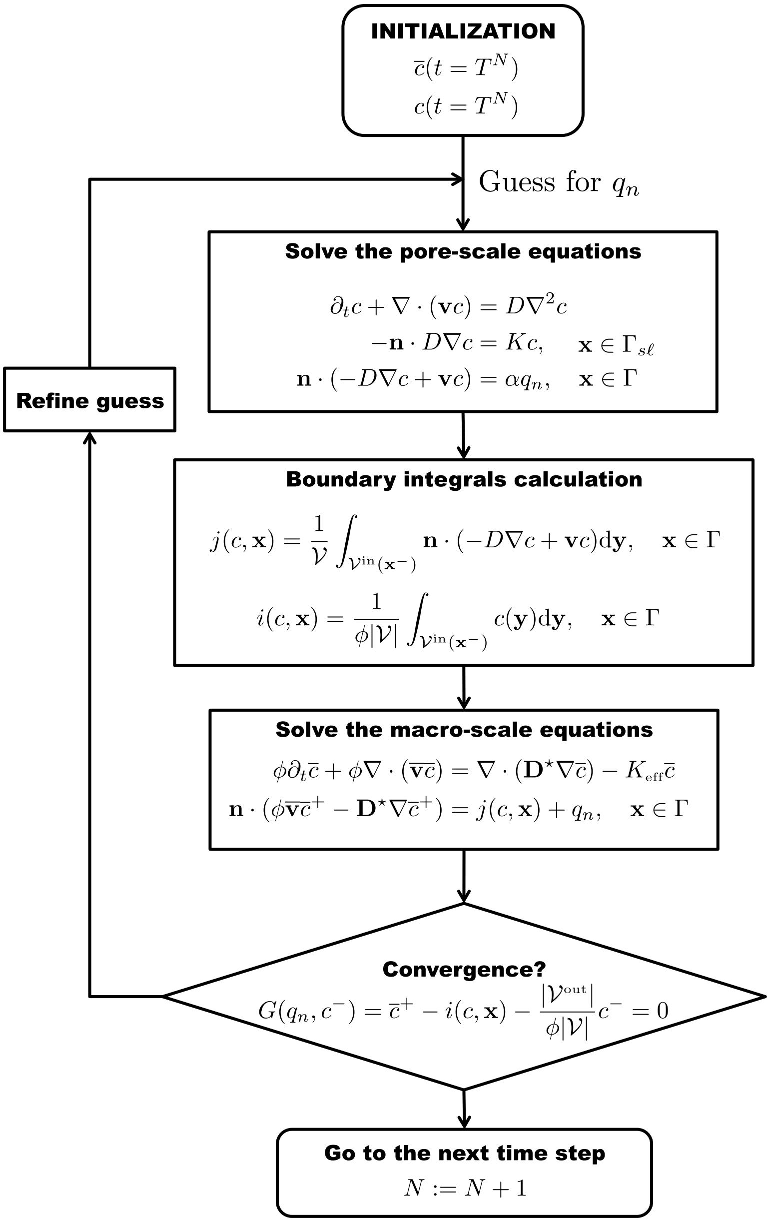

Fig. 3. Algorithm flowchart.

and the Péclet (Pe_y) and Damköhler (Da_y) numbers are defined as

$$\mathrm{Pe}_y := \frac{u_m L}{2D}, \quad \text{and} \quad \mathrm{Da}_y := \frac{\mathcal{K}L}{2D}. \tag{28}$$

Equation (26) is only valid when the system is well mixed at the pore-scale, i.e. across a vertical cross-section. This is attained when, e.g., $\mathrm{Da}_y < 1$; constraints on the order of magnitude of Pe_y number also exist [13]. Whenever one, or more, of such constraints is violated in a subdomain $\mathbf{x} := (x, y) \in \overline{\Omega}_p$ of the channel, e.g. for $x \in \{x_1, x_2\}$ and $y = \{0, L\}$, then the hybrid coupled system (20) reduces to

$$\partial_t c + u(y)\partial_x c - D(\partial^2_{xx} c + \partial^2_{yy} c) = 0, \qquad \mathbf{x} \in \overline{\Omega}_p, \tag{29a}$$

$$-D\partial_y c = \mathcal{K}c, \qquad x \in \{x_1, x_2\}, \; y = 0 \tag{29b}$$

$$D\partial_y c = \mathcal{K}c, \qquad x \in \{x_1, x_2\}, \; y = L \tag{29c}$$

$$D\partial_x c - uc = q_W, \qquad x \in \Gamma_W \tag{29d}$$

Table 1
Fracture domain.

Fracture length, L_t	[L]	20
Fracture aperture, L	[L]	0.25
Pore-scale domain length, l_x	[L]	0.25

Table 2
Pore-scale domain parameters of the fracture.

Grid size (x-direction), Δx	[L]	0.012
Grid size (y-direction), Δy	[L]	0.012
Time step, Δt	[T]	10^{-6}
Diffusion coefficient, D	[$\mathrm{L}^2\,\mathrm{T}^{-1}$]	20
Maximum velocity, u_m	[$\mathrm{L}\mathrm{T}^{-1}$]	15
Péclet number, Pe_y	[–]	≈ 0.1
Reaction coefficient	[T^{-1}]	
Case 1		$\mathcal{K}=0$ $(\mathrm{Da}_y=0)$
Case 2		$\mathcal{K}=5$ $(\mathrm{Da}_y\approx 0.03)$
Case 3		$\mathcal{K}_1=5$, $\mathcal{K}_2=450$ $(\mathrm{Da}_{y1}=0.03)$, $(\mathrm{Da}_{y2}=2.8)$

$$-D\partial_x c + uc = q_E, \qquad x\in\Gamma_E \tag{29e}$$

$$\partial_t\overline{c} + U\partial_x\overline{c} - D^\star\partial^2_{xx}\overline{c} + K^\star\overline{c} = 0 \qquad x\in\Omega\setminus\overline{\Omega}_p \tag{29f}$$

$$\overline{c}^+ = c^- \qquad x\in\Gamma=\{\Gamma_W,\Gamma_E\} \tag{29g}$$

$$(\phi U\overline{c}^+ - D^\star\partial_x\overline{c}^+) = q_W \qquad x\in\Gamma_W \tag{29h}$$

$$(-\phi U\overline{c}^+ + D^\star\partial_x\overline{c}^+) = q_E \qquad x\in\Gamma_E \tag{29i}$$

where Γ_W and Γ_E represent the west and east (vertical) boundaries between the pore- and continuum-scale domains, and q_W and q_E their corresponding (unknown) fluxes. Equations (22) simplify to

$$G(q_n, c^-) = \overline{c}^+ - c^-, \tag{30a}$$

$$F(q_n, c^-) = \mathbf{n}\cdot(\phi U\overline{c}^+ - D^\star\nabla\overline{c}^+) - q_n. \tag{30b}$$

3.1. Validation: transport in a chemically homogeneous channel

We model advective–diffusive transport in a channel with both (i) no reaction, i.e. $K^\star = 0$ (Case 1) and (ii) homogeneous surface reaction rate, i.e. $K^\star = \text{const} \neq 0$ (Case 2) as benchmark problems to validate the hybrid coupling (29). In both scenarios the continuum-scale equation admits an analytical solution, which we use to validate the accuracy of the hybrid algorithm. The analytical solution of (26) supplemented by the initial and boundary conditions

$$\overline{c}(x,0)=1, \qquad \overline{c}(0,t)=0, \qquad \frac{\partial\overline{c}}{\partial x}(\infty,t)=0, \tag{31}$$

is

$$\overline{c}(x,t) = \frac{1}{2}\exp(K^\star t)\left[2-\exp\left(\frac{Ux}{D^\star}\right)\mathrm{erf}\left(\frac{x+Ut}{2\sqrt{D^\star t}}\right)+\mathrm{erf}\left(\frac{x-Ut}{2\sqrt{D^\star t}}\right)\right], \tag{32}$$

where $K^\star = 0$ or $K^\star = \text{const} \neq 0$. The parameters used in the simulations are summarized in Tables 1, 2 and 3 (Cases 1 and 2). These simulations are used (i) to perform a grid and time-step study to confirm that the spatial and temporal discretization are capable to provide sufficient accuracy and (ii) to validate the accuracy of the hybrid model. Figs. 4 and 5 show a perfect agreement between the analytical and hybrid solutions.

In Section 3.2, we use our hybrid model for a localized highly reaction rate. The comparison between hybrid, Darcy-scale and pore-scale solutions is presented.

3.2. Transport in a chemically heterogeneous channel

We test the hybrid algorithm's capability and performance in handling chemical heterogeneity. We consider reactive transport in a chemically heterogeneous channel where a portion of the channel's walls is characterized by a reaction rate $\mathcal{K}_2$ two orders of magnitude larger than the reaction rate in the rest of the channel $\mathcal{K}_1$ (see Fig. 6(a)). We compare the vertically averaged fully 2D pore-scale solution with (i) the solution of the 1D macroscopic model (26) with spatially

Table 3
Continuum-scale domain parameters of the fracture.

Grid size (x-direction), ΔX	[L]	0.25
Time step, ΔT	[T]	$3 \cdot 10^{-4}$
Diffusion coefficient, $D^\star$	[$\mathrm{L^2 T^{-1}}$]	20.0015
Mean velocity, U	[$\mathrm{LT^{-1}}$]	10.0417
Péclet number, Pe	[–]	≈ 10
Reaction coefficient	[$\mathrm{LT^{-1}}$]	
Case 1		$K^\star = 0$ ($\mathrm{Da} = 0$)
Case 2		$K^\star = 39.55$ ($\mathrm{Da} \approx 40$)
Case 3		$K_1^\star = 39.55$, $K_2^\star = 225$ ($\mathrm{Da}_1 \approx 40$), ($\mathrm{Da}_2 \approx 225$)

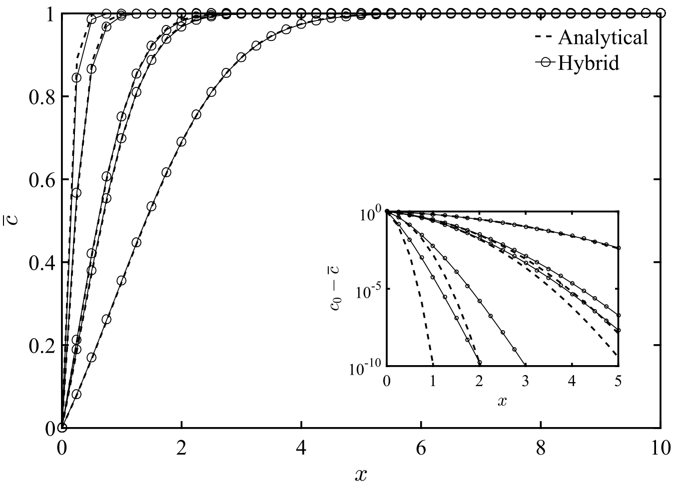

Fig. 4. Case 1: $K^\star = 0$. The average concentration $\bar{c}$ obtained from the hybrid algorithm (solid line with empty circles) compared with the analytical solution (43) (dashed line) at times $t = 0.0006$, $t = 0.0024$, $t = 0.015$, $t = 0.018$, $t = 0.06$ (from left to right).

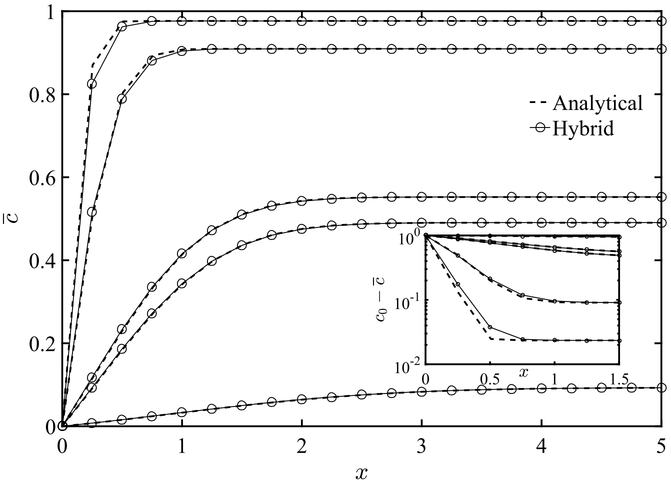

Fig. 5. Case 2: $K^\star = 39.55$. The average concentration $\bar{c}$ obtained from the hybrid algorithm (solid line with empty circles) compared with the analytical solution (43) (dashed line) at times $t = 0.0006$, $t = 0.0024$, $t = 0.015$, $t = 0.018$, $t = 0.06$ (from top to bottom).

heterogeneous reaction rates $K_1^\star$ and $K_2^\star$ (Case 3 in Table 3, Fig. 6(b)) and (ii) the hybrid model (Fig. 6(c)). The parameters of the pore-scale and continuum-scale simulations are listed in Tables 2 and 3, respectively. We emphasize that, despite $\mathcal{K}_2$ is selected such that $\mathrm{Da}_y < 3$ (i.e. the condition of applicability of the continuum model (26) is not violated), the 1D model fails to capture the macroscopic behavior of the concentration field in proximity of the heterogeneity, as apparent from Fig. 7. For $\mathrm{Da}_y < 3$, $K^\star$ and $\mathcal{K}$ have the same sign and, as a result, the upscaled and spatially averaged pore-scale models

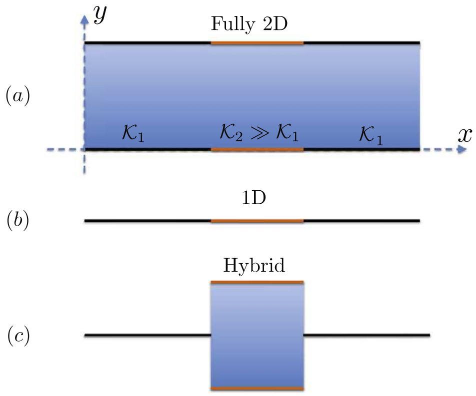

Fig. 6. A schematic representation of a fracture with heterogeneous reactive walls. One portion of the fracture (in orange) is much more reactive than the rest. (For interpretation of the references to color in this figure legend, the reader is referred to the web version of this article.)

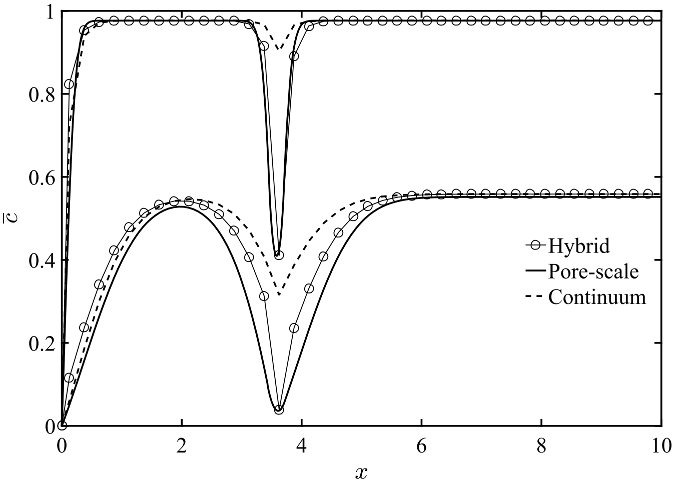

Fig. 7. Case 3: The average concentration compared with the 1D continuum model (solid line), hybrid solution (solid line with empty circles) and fully resolved 2D (dashed line) at times $t = 0.0006$, $t = 0.015$ (from top to bottom).

exhibit the same trend in the average concentration $\bar{c}$. Yet, the accuracy of the macroscale model quickly deteriorates as one approaches $\mathrm{Da}_y = 3$. In particular, the upscaled equation significantly overestimates the average concentration. The hybrid model, on the other hand, is able to capture the average concentration field throughout the domain. Increasing deviations of the hybrid solution from the upscaled 2D model can be attributed to the expansion of the reacting front beyond the (fixed) boundaries of the pore-scale domain in the hybrid algorithm, as shown in Fig. 8.

The computation time for 1D continuum, hybrid and pore 2D simulations was 1.2, 1.98×10 and 9.88×10^2 seconds, respectively. This corresponds to a ~ 50 times computational speed up compared to fully 2D simulations when employing the hybridization. The number of iterations is generally around 40–50 for the first time steps and reduces to 2–3 after few time steps.

Fig. 9 shows the difference between the pore-scale concentration distribution at the hybridization location in the 2D and hybrid algorithms. The two concentrations compare well. This suggests that the hybrid model not only is able to predict the average concentration, but also the micro-scale (i.e. pore-scale) behavior at the breakdown site.

We refer to any model as *predictive* if the error is bounded by an *a priori* known criterion. Homogenization/upscaling imposes that the upscaling error should be bounded by ϵ [12–14]. Fig. 10 shows the absolute error of the upscaled and the hybrid models at time $t = 0.06$. As expected, the error in the hybrid algorithm is bounded by $\epsilon = L/L_t = 1.25 \times 10^{-2}$, i.e. it is bounded by the theoretical upscaling/modeling error prescribed by homogenization theory [13]. In other words, the order of magnitude of the error introduced through the coupling process should not overshoot the upscaling error in the macroscopic model. This is not the case for the 1D upscaled model, even though its applicability conditions are not violated. Fig. 10 shows that the maximum error takes place in the coupling node.

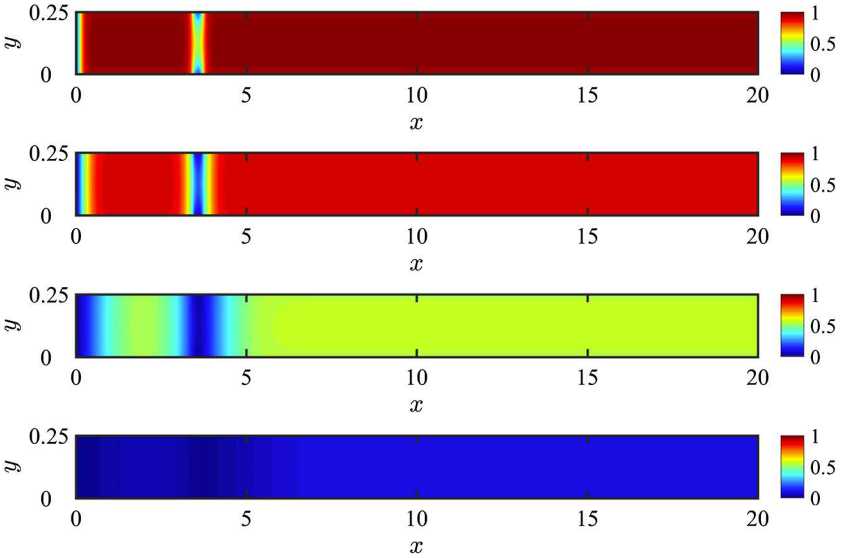

Fig. 8. Case 3: Pore-scale concentration obtained from fully resolved 2D equations at times $t = 0.0006$, $t = 0.0024$, $t = 0.015$, $t = 0.06$ (top to bottom).

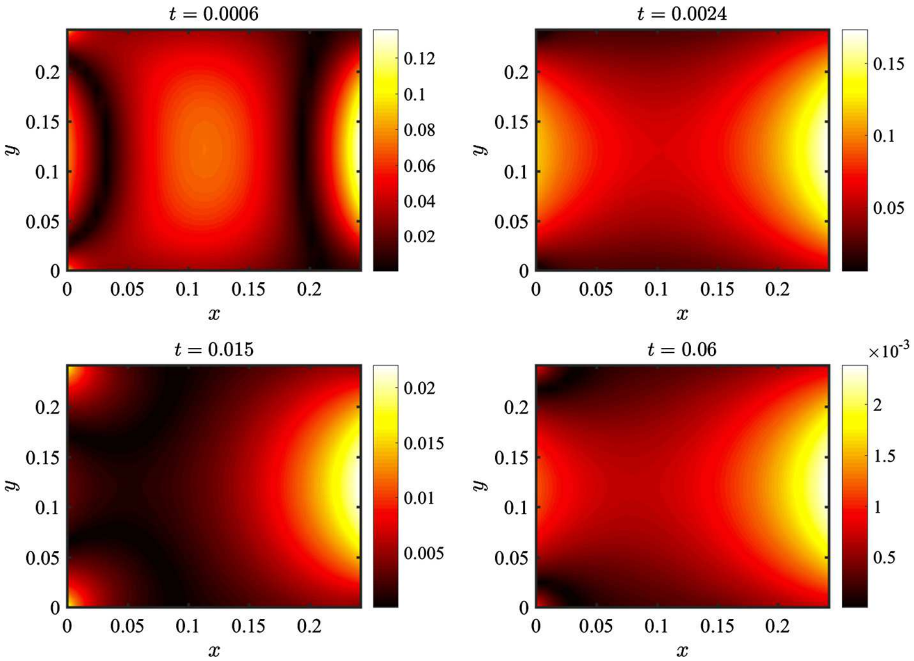

Fig. 9. Absolute error of the concentration field at the hybridization location in the hybrid algorithm at times $t = 0.0006$, $t = 0.0024$, $t = 0.015$, and $t = 0.06$ (Table 3, Case 3).

4. Transport past an array of cylindrical solid obstacles

To test the hybrid algorithm performance on transport through a more complex geometry, we consider flow and transport past an array of reactive cylinders inside a channel of width L_y. The domain contains 40 reactive cylinders. The reaction rate on the surface of two cylinders is selected beyond the validity range of the upscaled equation, specifically $\mathrm{Da}_2 = 2$ (i.e. $\mathcal{K}_2 = 2$). The rest of the cylinders are characterized by $\mathrm{Da}_1 = 0.1$ (i.e. $\mathcal{K}_1 = 0.1$). The steady state Navier–Stokes equations (1) are solved using implicit Immersed Boundary Method techniques [46]. The pore-scale transport equation (3) subject to (4) is discretized on a Cartesian staggered grid using a variation of QUICK scheme [47]. The reactive boundary condition is imposed using the Immersed Boundary Method [46]. We assume uniform concentration distribution at $t = 0$, and a Dirichlet boundary condition at the inlet, $c(0, y, t) = 0$. The discretized equations are solved implicitly using the Bi-conjugate gradient stabilized method [48]. All simulation parameters are summarized in Tables 4–6. The equations of the hybrid algorithm are

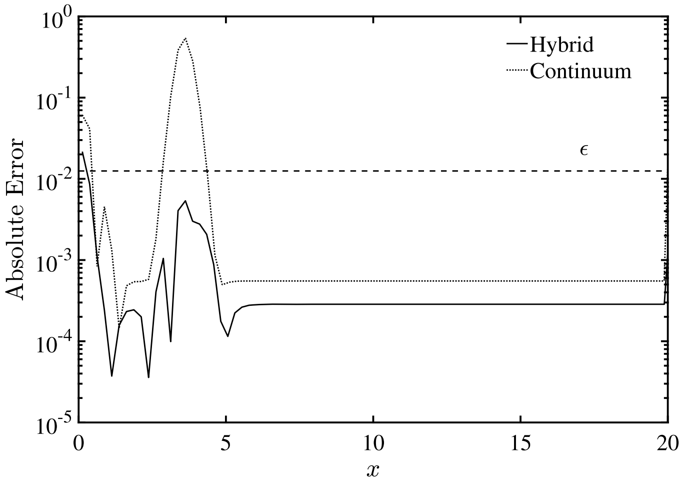

Fig. 10. Absolute error along the fracture in the 1D and hybrid models at $t = 0.0024$ (Case 3, Table 3). Unlike the upscaled solution, the hybrid model has an error lower than the theoretical bound ϵ.

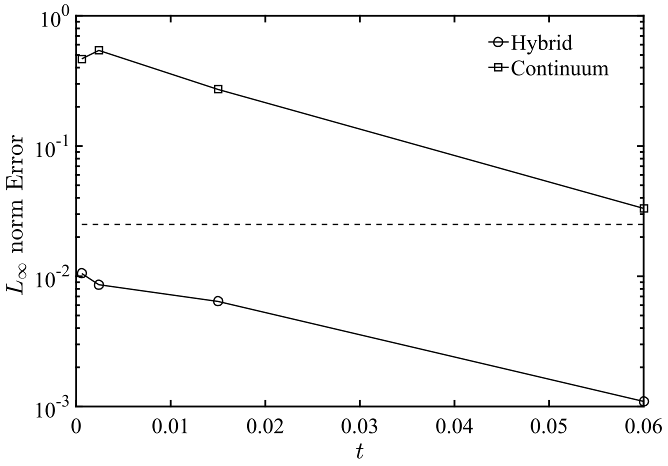

Fig. 11. The L_∞ norm error versus time in the continuum 1D (solid lines with squares) and the hybrid (solid lines with circles) solutions. Unlike the 1D model, the modeling error of the hybrid model is always below the upscaling error. The reduction of the error with time is due to the consumption of the total mass in the fracture.

$$\partial_t c + u\partial_x c + v\partial_y c = D(\partial^2_{xx}c + \partial^2_{yy}c), \quad \mathbf{x}\in\overline{\Omega}_p, \tag{33a}$$

$$-\mathbf{n}\cdot D\nabla c = \mathcal{K}c, \quad \mathbf{x}\in\Gamma_{s\ell}, \tag{33b}$$

$$D\partial_x c - uc = q_W, \quad \mathbf{x}\in\Gamma_W, \tag{33c}$$

$$-D\partial_y c + uc = q_E, \quad \mathbf{x}\in\Gamma_E, \tag{33d}$$

$$\phi\partial_t\bar{c} + U\partial_x\bar{c} = D^\star\partial^2_{xx}\bar{c} - K^\star\bar{c}, \quad \mathbf{x}\in\Omega\setminus\overline{\Omega}_p, \tag{33e}$$

$$\mathbf{n}\cdot(\phi\overline{\mathbf{v}c}^+ - \mathbf{D}^\star\nabla\bar{c}^+) = j(c,\mathbf{x}) + q_n,\ q_n = \{q_E, q_W\} \quad \mathbf{x}\in\Gamma, \tag{33f}$$

$$G(q_E, q_W, c^-) = \bar{c}^+ - i(c,\mathbf{x}) - \frac{c(\mathbf{x}^-)}{\alpha\phi} = 0, \quad \mathbf{x}\in\Gamma, \tag{33g}$$

where u and v are the horizontal and vertical component of the velocity field $\mathbf{v}$, $\alpha = |\mathcal{V}|/|\mathcal{V}^{\text{out}}|$, $j(c,\mathbf{x})$ and $i(c,\mathbf{x})$ are defined by (21). The coupling volume $\mathcal{V}$ is a rectangle containing two cylinders; its partitions $\mathcal{V}^{\text{in}}$ and $\mathcal{V}^{\text{out}}$ are depicted in Fig. 12. We compare the fully 2D solution, the coupled 2D–1D model (hybrid model) and the 1D solutions. The concentration from the fully 2D solution spatially averaged over $\mathcal{V}$ is used as the reference for comparison.

In Fig. 13, we plot the average concentration distribution at two instances in time for the three different models. While the 1D continuum model significantly underestimates the average concentration in the portion of the domain where the highly reactive cylinders are located, the match between the hybrid solution and the spatially averaged 2D solution is excellent. Fig. 14 shows the pore-scale concentration distribution in the fully resolved model. Fig. 15 shows the absolute

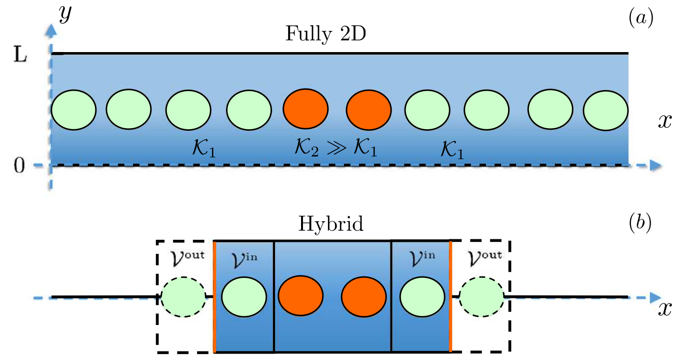

Fig. 12. (a) Pore-scale schematic representation of flow past an array of heterogeneous reactive obstacles. (b) Schematics of the hybrid (pore-scale/continuum) coupling domain.

Table 4
Cylindrical obstacles geometry.

Cylinder diameter, d	[L]	1
Fracture aperture (y-direction), L	[L]	3
Fracture length (x-direction), L_t	[L]	120
Number of cylinders, n	[−]	40
Distance between cylinders centers, L_c	[L]	3

Table 5
Pore-scale domain parameters for transport past cylindrical obstacles.

Grid size (x-direction), Δx	[L]	0.05
Grid size (y-direction), Δy	[L]	0.05
Time step, Δt	[T]	$5 \cdot 10^{-4}$
Diffusion coefficient, D	[$\mathrm{L}^2\,\mathrm{T}^{-1}$]	1
Uniform inlet velocity, u_m	[LT^{-1}]	1
Reaction coefficient, $\mathcal{K}_1$	[LT^{-1}]	0.1
Reaction coefficient, $\mathcal{K}_2$	[LT^{-1}]	2

Table 6
Continuum-scale domain parameters for transport past cylindrical obstacles.

Grid size (x-direction), ΔX	[L]	0.33
Time step, Δt	[T]	0.01
Dispersion coefficient, $D^\star$	[$\mathrm{L}^2\,\mathrm{T}^{-1}$]	1.014
Uniform inlet velocity, u_m	[LT^{-1}]	1
Reaction coefficient, $K_1^\star$	[LT^{-1}]	0.03723

difference between the pore-scale concentration distribution at the hybridization location in the fully resolved solution and hybrid algorithm. The two values compare well. This again verifies that the hybrid model not only is able to predict the average concentration within expected error bound, but also the micro-scale (i.e. pore-scale) behavior at the breakdown site. More quantitatively, Fig. 16 shows a comparison between the errors of the 1D upscaled and the 1D/2D hybrid models along the fracture at a fixed instant in time. The error of the macroscopic model significantly overshoots the upscaling error bound in the highly reactive zone. Instead, the hybrid performs much better with the error bounded by ϵ in the coupling location. Both models show high errors at the inlet, where sharp concentration gradients are generated by the Dirichlet boundary condition, and are not accommodated by an appropriate pore-scale model. In Fig. 17, we plot the L_∞ norm error in the 1D and hybrid models for the entire simulation time. Similarly to what observed earlier, while the modeling error of the 1D model always overcomes the theoretical bound ϵ imposed by the homogenization technique, the modeling error in the hybrid is bounded by ϵ for the entire simulation time. The increase of the hybrid model error with time is due to the propagation of the reacting front beyond the hybridization domain, which calls for adaptive hybridization schemes. For completeness, we show a schematic representation of a 2D hybrid model in Fig. 18.

5. Conclusions

We introduced a novel non-overlapping tightly coupled hybrid algorithm to model reactive transport in fractured and porous media. Unlike many multiscale formulations based on purely numerical coupling techniques, the proposed coupling conditions are physics-based and obtained by means of mathematical upscaling tools. As a result, the coupling error is

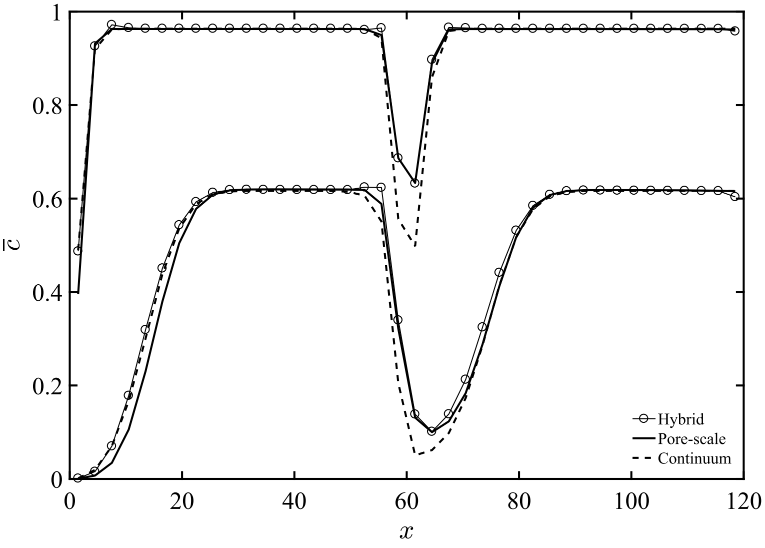

Fig. 13. The average concentration obtained from the 1-D continuum model, hybrid solution and fully resolved 2-D at times $t = 1$ and $t = 13$.

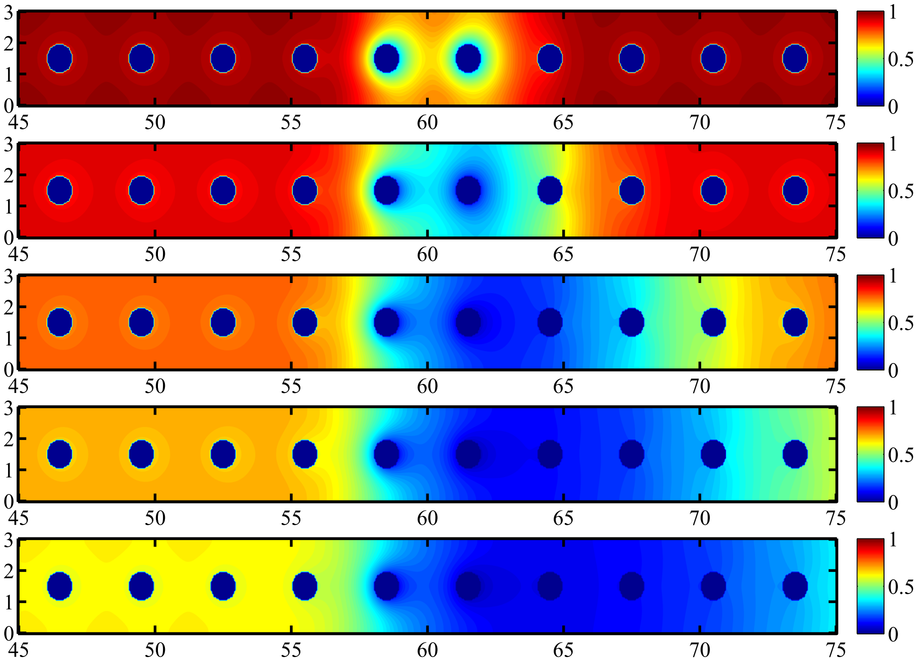

Fig. 14. Pore-scale concentration of the fully 2D solution at times $t = 1$, $t = 3$, $t = 7$, $t = 10$, and $t = 13$ (top to bottom).

bounded by the upscaling error, and the multiscale model can be defined predictive. Furthermore, the method shares similar advantages with other multiscale schemes based on domain decomposition approaches, including the lack of an overlapping region and straightforward implementation in legacy and existing codes. Like most of the hybrid methods, the algorithm does not depend on prior familiarity of the parameters beside continuum properties of porous media, pore-scale domain geometry, and chemical and physical properties of the solute and fluid.

The coupling is based on an iterative algorithm in which the fluxes into the pore-scale domain are unknown. The algorithm reduces to a zero finding problem for a vector function whose components are the unknown fluxes. We implemented the algorithm to simulate the transport of a solute in a fracture and past an arrays of cylinders with highly localized heterogeneity in reaction rates. We show that the coupling errors are bounded by the upscaling errors, if the pore-scale model is solved whenever the continuum-scale equations fails. While we used a finite volumes method to implement the test cases, the coupling algorithm is general and can be formulated using any other numerical discretization scheme. The iterative

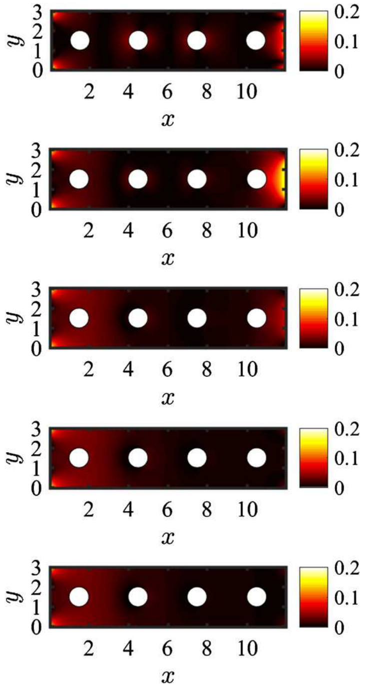

Fig. 15. Absolute error the pore-scale concentration at the hybridization location in the multiscale model and the fully 2D solution at times $t = 1$, $t = 3$, $t = 7$, $t = 10$, and $t = 13$ (top to bottom). As expected, the error is higher at the coupling locations (left and right boundaries).

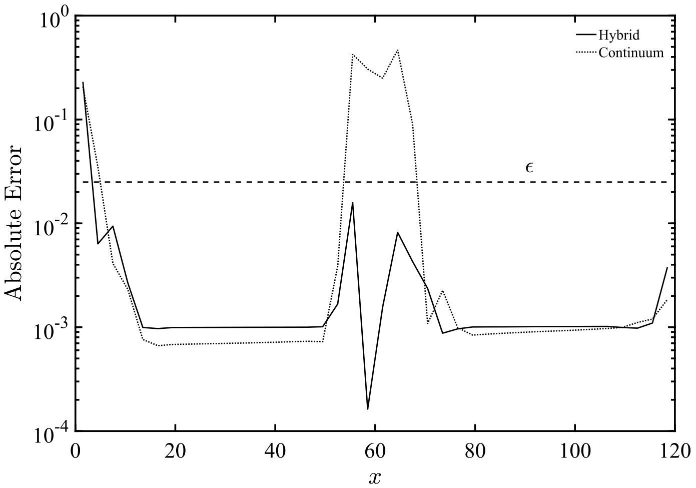

Fig. 16. Maximum error of the 1D (solid lines with squares) and hybrid models (solid lines with circles) in terms of the longitudinal distance along the channel at time $t = 1$. The dashed line represents the homogenization/upscaling theoretical error ϵ.

nature of the hybrid model requires a root finding algorithm. We employed Broyden's method. The convergence rate of and accuracy of the algorithm may be improved by utilizing different zero finding algorithms.

In follow-up studies, we (i) will test the performance of the proposed hybrid algorithm to model reactive transport in realistic pore geometries and (ii) will implement it into current commercial CFD codes.

Acknowledgements

The authors would like to thank the insightful comments by two anonymous Referees and Alberto Guadagnini. The alternative and more compact derivation of (A.14) and (A.15) was kindly proposed by Referee 1. Support from the National Science Foundation award number 1742569 is gratefully acknowledged.

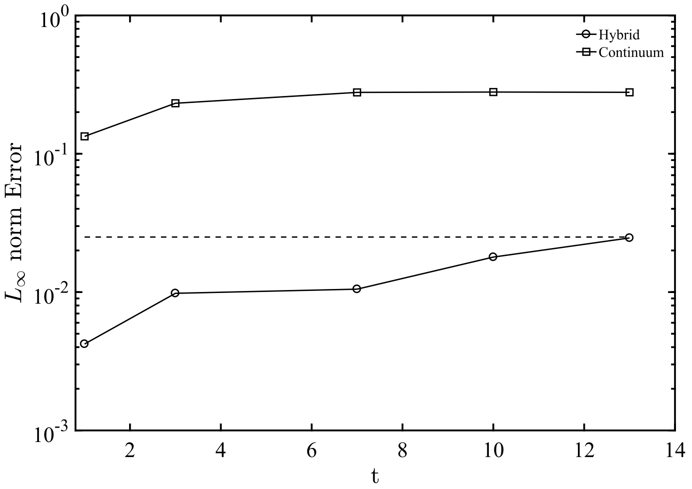

Fig. 17. L_∞ norm error versus time in the continuum 1D (solid line with squares) and the hybrid (solid line with circles) solutions. While the modeling error of the 1D model always overcomes the theoretical bound ϵ imposed by the homogenization technique, the modeling error in the hybrid is bounded by ϵ for the entire simulation time. The increase of the hybrid model error with time is due to the propagation of the reacting front beyond the hybridization domain.

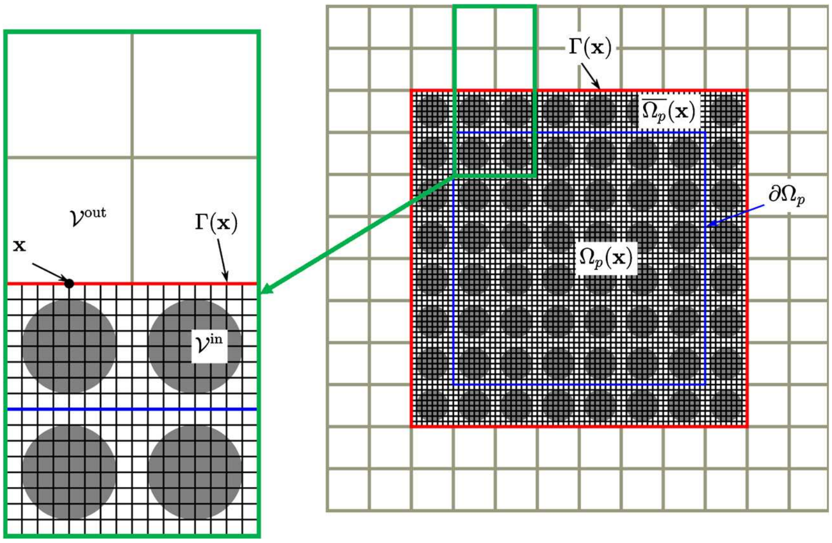

Fig. 18. Schematic representation of a hybrid domain in a 2D continuum problem.

Appendix A. Derivation of flux continuity boundary condition

In order to derive a flux continuity coupling boundary, we start by averaging (20a), i.e.

$$\phi\partial_t\bar{c} + \phi\overline{\nabla\cdot(-D\nabla c + \mathbf{v}c)} = 0. \tag{A.1}$$

Invoking the spatial averaging theorem

$$\langle\nabla u\rangle = \nabla\langle u\rangle + \frac{1}{|\mathcal{V}|}\int_{\Gamma_{s\ell}} u\mathbf{n}\mathrm{d}\Gamma, \tag{A.2}$$

Equation (A.1) can be written as

$$\phi\overline{\nabla\cdot(-D\nabla c + \mathbf{v}c)} = \phi\nabla\cdot\overline{(-D\nabla c + \mathbf{v}c)} + \frac{\phi}{|\mathcal{V}|}\int_{\Gamma_{s\ell}}(-D\nabla c + \mathbf{v}c)\mathbf{n}\mathrm{d}\Gamma. \tag{A.3}$$

Accounting for the reactive boundary condition (4) and the no-slip condition on the solid–liquid boundaries $\Gamma_{s\ell}$, one obtains

$$\phi\overline{\nabla\cdot(-D\nabla c+\mathbf{v}c)}=\phi\nabla\cdot\overline{(-D\nabla c+\mathbf{v}c)}+\frac{\phi}{|\mathcal{V}|}\int\limits_{\Gamma_{s\ell}}\mathcal{K}c\mathbf{n}\mathrm{d}\Gamma. \tag{A.4}$$

Inserting (A.4) into (A.1) leads to

$$\phi\frac{\partial\bar{c}}{\partial t}+\phi\nabla\cdot\overline{(-D\nabla c+\mathbf{v}c)}+\frac{\phi}{|\mathcal{V}|}\int\limits_{\Gamma_{s\ell}}\mathcal{K}c\mathbf{n}\mathrm{d}\Gamma=0. \tag{A.5}$$

Integrating (A.5) over an arbitrary volume J containing Γ (the boundary of the enlarged domain $\overline{\Omega}_p$, see Fig. 2) leads to

$$\begin{aligned}\phi\frac{\partial}{\partial t}\int\limits_{J}\bar{c}\mathrm{d}\mathbf{y}=&-\phi\int\limits_{J_{in}}\nabla\cdot\overline{(-D\nabla c+\mathbf{v}c)}\mathrm{d}\mathbf{y}-\phi\int\limits_{J_{out}}\nabla\cdot\overline{(-D\nabla c+\mathbf{V}c)}\mathrm{d}\mathbf{y}\\&-\frac{\phi}{|J||\mathcal{V}|}\int\limits_{J_{out}}\int\limits_{\Gamma_{s\ell}}\mathcal{K}c\mathrm{d}\Gamma-\frac{\phi}{|J||\mathcal{V}|}\int\limits_{J_{in}}\int\limits_{\Gamma_{s\ell}}\mathcal{K}c\mathrm{d}\Gamma\end{aligned} \tag{A.6}$$

where J_{in} and J_{out} are the partitions of J, i.e. $J=J_{in}\cup J_{out}$ and $J_{in}=J\cap\overline{\Omega}_p$. Since in J_{out} the upscaled model holds, then

$$\begin{aligned}\phi\frac{\partial}{\partial t}\int\limits_{J}\bar{c}\mathrm{d}\mathbf{y}=&-\phi\int\limits_{J_{in}}\nabla\cdot\overline{(-D\nabla c+\mathbf{v}c)}\mathrm{d}\mathbf{y}-\int\limits_{J_{out}}\nabla\cdot(-D^{\star}\nabla\bar{c}+\phi\mathbf{V}\bar{c})\mathrm{d}\mathbf{y}\\&-\frac{\phi}{|J||\mathcal{V}|}\int\limits_{J_{out}}\int\limits_{\Gamma_{s\ell}}\mathcal{K}c\mathrm{d}\Gamma-\frac{\phi}{|J||\mathcal{V}|}\int\limits_{J_{in}}\int\limits_{\Gamma_{s\ell}}\mathcal{K}c\mathrm{d}\Gamma.\end{aligned} \tag{A.7}$$

Using the Gauss's integral theorem, while observing that J_{in} and J_{out} are bounded by $\Gamma_{in}\cup\Gamma_J$ and $\Gamma_{out}\cup\Gamma_J$, respectively, where $\Gamma_{in}=\partial J\cap\overline{\Omega}_p$, $\Gamma_{out}=\partial J\backslash\Gamma_{in}$, $\Gamma_J=J\cap\Gamma$, gives

$$\begin{aligned}\phi\frac{\partial}{\partial t}\int\limits_{J}\bar{c}\mathrm{d}\mathbf{y}=&-\phi\int\limits_{\Gamma_{in}}\mathbf{n}\cdot\overline{(-D\nabla c+\mathbf{v}c)}\mathrm{d}\mathbf{y}-\int\limits_{\Gamma_{out}}\mathbf{n}\cdot(\phi\mathbf{V}\bar{c}-D^{\star}\nabla\bar{c})\mathrm{d}\mathbf{y}\\&-\frac{\phi}{|J||\mathcal{V}|}\int\limits_{J_{in}}\int\limits_{\Gamma_{s\ell}}\mathcal{K}c\mathrm{d}\Gamma-\frac{\phi}{|J||\mathcal{V}|}\int\limits_{J_{out}}\int\limits_{\Gamma_{s\ell}}\mathcal{K}c\mathrm{d}\Gamma\\&-\phi\int\limits_{\Gamma_J}\mathbf{n}\cdot\overline{(-D\nabla c+\mathbf{v}c)}\mathrm{d}\mathbf{y}+\int\limits_{\Gamma_J}\mathbf{n}\cdot(\phi\mathbf{V}\bar{c}-D^{\star}\nabla\bar{c})\mathrm{d}\mathbf{y}.\end{aligned} \tag{A.8}$$

Rewriting the LHS of (A.6) leads to

$$\phi\frac{\partial}{\partial t}\int\limits_{J}\bar{c}\mathrm{d}\mathbf{y}=-\phi\int\limits_{J}\nabla\cdot\overline{(-D\nabla c+\mathbf{v}c)}\mathrm{d}\mathbf{y}-\frac{\phi}{|J||\mathcal{V}|}\int\limits_{J}\int\limits_{\Gamma_{s\ell}}\mathcal{K}c\mathrm{d}\Gamma. \tag{A.9}$$

Applying the Gauss's integral theorem, one obtains

$$\phi\frac{\partial}{\partial t}\int\limits_{J}\bar{c}\mathrm{d}\mathbf{y}=-\phi\int\limits_{\Gamma_{in}}\mathbf{n}\cdot\overline{(-D\nabla c+\mathbf{v}c)}\mathrm{d}\mathbf{y}-\phi\int\limits_{\Gamma_{out}}\mathbf{n}\cdot\overline{(-D\nabla c+\mathbf{v}c)}\mathrm{d}\mathbf{y}-\frac{\phi}{|J||\mathcal{V}|}\int\limits_{J}\int\limits_{\Gamma_{s\ell}}\mathcal{K}c\mathrm{d}\Gamma. \tag{A.10}$$

Subtracting (A.10) from (A.8), one obtains

$$\begin{aligned}&-\phi\int\limits_{\Gamma_J}\mathbf{n}\cdot\overline{(-D\nabla c+\mathbf{v}c)}\mathrm{d}\mathbf{y}+\int\limits_{\Gamma_J}\mathbf{n}\cdot(\phi\mathbf{V}\bar{c}-\mathbf{D}^{\star}\nabla\bar{c})\mathrm{d}\mathbf{y}\\&+\phi\int\limits_{\Gamma_{out}}\mathbf{n}\cdot\overline{(-D\nabla c+\mathbf{v}c)}\mathrm{d}\mathbf{y}-\int\limits_{\Gamma_{out}}\mathbf{n}\cdot(\phi V\bar{c}-\mathbf{D}^{\star}\nabla\bar{c})\mathrm{d}\mathbf{y}=0\end{aligned} \tag{A.11}$$

or, if ϕ is constant,

$$\int_{\Gamma_J} \left[-\phi \mathbf{n} \cdot \overline{(-D\nabla c + \mathbf{v}c)} + \mathbf{n} \cdot (\phi \mathbf{V}\overline{c} - D^{\star} \nabla \overline{c}) \right] \mathrm{d}\mathbf{y}$$
$$+ \int_{\Gamma_{out}} \left[\phi \mathbf{n} \cdot \overline{(-D\nabla c + \mathbf{v}c)} \mathrm{d}\Gamma - \mathbf{n} \cdot (\phi \mathbf{V}\overline{c} - D^{\star} \nabla \overline{c}) \right] \mathrm{d}\mathbf{y} = 0. \tag{A.12}$$

Since the integral on Γ_{out} is identically zero, this leads to the second coupling condition

$$\mathbf{n} \cdot \phi \overline{(-D\nabla c + \mathbf{v}c)}^{-} = \mathbf{n} \cdot (\phi \mathbf{V}\overline{c}^{+} - \mathbf{D}^{\star} \nabla \overline{c}^{+}). \tag{A.13}$$

The same result could be more elegantly derived by observing that

$$\phi \int_{J_{out}} \nabla \cdot \overline{(-D\nabla c + \mathbf{V}c)} \mathrm{d}\mathbf{y} = \int_{J_{out}} \nabla \cdot (-D^{\star} \nabla \overline{c} + \phi \mathbf{V}\overline{c}) \mathrm{d}\mathbf{y}. \tag{A.14}$$

Using the Gauss integral theorem yields,

$$\phi \int_{\Gamma_{out}} \mathbf{n} \cdot \overline{(-D\nabla c + \mathbf{V}c)} \mathrm{d}\mathbf{y} + \phi \int_{\Gamma_J} \mathbf{n} \cdot \overline{(-D\nabla c + \mathbf{V}c)} \mathrm{d}\mathbf{y}$$
$$= \int_{\Gamma_{out}} \mathbf{n} \cdot (-D^{\star} \nabla \overline{c} + \phi \mathbf{V}\overline{c}) \mathrm{d}\mathbf{y} + \int_{\Gamma_J} \mathbf{n} \cdot (-D^{\star} \nabla \overline{c} + \phi \mathbf{V}\overline{c}) \mathrm{d}\mathbf{y}, \tag{A.15}$$

that is equivalent to (A.11).

References

[1] R.E. García, Y.M. Chiang, W.C. Carter, P. Limthongkul, C.M. Bishop, Microstructural modeling and design of rechargeable lithium-ion batteries, J. Electrochem. Soc. 152 (2005) A255.

[2] H. Arunachalam, S. Onori, I. Battiato, On veracity of macroscopic lithium-ion battery models, J. Electrochem. Soc. 162 (10) (2015) A1940–A1951.

[3] R. García-García, R.E. García, Microstructural effects on the average properties in porous battery electrodes, J. Power Sources 309 (2016) 11–19.

[4] X. Zhang, D.M. Tartakovsky, Effective ion diffusion in charged nanoporous materials, J. Electrochem. Soc. 164 (4) (2017).

[5] T.-S. Wong, S. Kang, S. Tang, E. Smythe, B. Hatton, A. Grinthal, J. Aizenberg, Bioinspired self-repairing slippery surfaces with pressure-stable omniphobicity, Nature 477 (2011) 443–447.

[6] I. Battiato, Effective medium theory for drag-reducing micro-patterned surfaces in turbulent flows, Eur. Phys. J. E 37 (3) (2014).

[7] A. Papke, I. Battiato, A reduced complexity model for dynamic similarity in obstructed shear flows, Geophys. Res. Lett. 40 (15) (2013) 3888–3892.

[8] I. Battiato, S. Rubol, Single-parameter model of vegetated aquatic flows, Water Resour. Res. 8 (2014) 6358–6369.

[9] S. Rubol, I. Battiato, F.P.J. de Barros, Vertical dispersion in vegetated shear flows, Water Resour. Res. 52 (10) (2016) 8066–8080.

[10] S. Weinbaum, X. Zhang, Y. Han, H. Vink, S.C. Cowin, Mechanotransduction and flow across the endothelial glycocalyx, Proc. Natl. Acad. Sci. USA 100 (2003) 7988.

[11] B. Ling, A.M. Tartakovsky, I. Battiato, Dispersion controlled by permeable surfaces: surface properties and scaling, J. Fluid Mech. 801 (2016) 13–42.

[12] I. Battiato, D.M. Tartakovsky, A.M. Tartakovsky, T. Scheibe, On breakdown of macroscopic models of mixing-controlled heterogeneous reactions in porous media, Adv. Water Resour. 32 (11) (2009) 1664–1673.

[13] I. Battiato, D. Tartakovsky, Applicability regimes for macroscopic models of reactive transport in porous media, J. Contam. Hydrol. 120 (2011) 18–26.

[14] F. Boso, I. Battiato, Homogenizability conditions for multicomponent reactive transport, Adv. Water Resour. 62 (2013) 254–265.

[15] H. Arunachalam, S. Onori, I. Battiato, Temperature-dependent multiscale-dynamics in lithium-ion battery electrochemical models, in: 2015 American Control Conference (ACC), IEEE, Piscataway, NJ, USA, 2015, pp. 305–310.

[16] M.A. Shannon, P.W. Bohn, M. Elimelech, J.G. Georgiadis, B.J. Marinas, A.M. Mayes, Science and technology for water purification in the coming decades, Nature 452 (2008) 301–310.

[17] M. Andreani, P. Gouze, L. Luquot, P. Jouanna, Changes in seal capacity of fractured claystone caprocks induced by dissolved and gaseous CO_2 seepage, Geophys. Res. Lett. 35 (2008) L14404.

[18] P.O. Mangane, L. Gouze, P. Gouze, L. Luquot, Permeability impairment of a limestone reservoir triggered by heterogeneous dissolution and particle migration during CO_2-rich injection, Geophys. Res. Lett. 17 (2013) 4114–4619.

[19] S. Taverniers, A.Y. Pigarov, D.M. Tartakovsky, Conservative tightly-coupled simulations of stochastic multiscale systems, J. Comput. Phys. 313 (2016) 400–414.

[20] A.M. Tartakovsky, D.M. Tartakovsky, T.D. Scheibe, P. Meakin, Hybrid simulations of reaction–diffusion systems in porous media, SIAM J. Sci. Comput. 30 (6) (2008) 2799–2816.

[21] M.T. Balhoff, K.E. Thompson, M. Hjortsø, Coupling pore-scale networks to continuum-scale models of porous media, Comput. Geosci. 33 (3) (2007) 393–410.

[22] Y. Mehmani, T. Sun, M. Balhoff, P. Eichhubl, S. Bryant, Multiblock pore-scale modeling and upscaling of reactive transport: application to carbon sequestration, Transp. Porous Media 95 (2) (2012) 305–326.

[23] I. Battiato, D.M. Tartakovsky, A.M. Tartakovsky, T.D. Scheibe, Hybrid models of reactive transport in porous and fractured media, Adv. Water Resour. 34 (9) (2011) 1140–1150.

[24] D. Roubinet, D.M. Tartakovsky, Hybrid modeling of heterogeneous geochemical reactions in fractured porous media, Water Resour. Res. 49 (12) (2013) 7945–7956.

[25] D.A. Barajas-Solano, A.M. Tartakovsky, Hybrid multiscale finite volume method for advection–diffusion equations subject to heterogeneous reactive boundary conditions, Multiscale Model. Simul. 14 (4) (2016) 1341–1376.

[26] F.J. Alexander, A.L. Garcia, D.M. Tartakovsky, Noise in algorithm refinement methods, Comput. Sci. Eng. 7 (3) (2005) 32–38.

[27] S. Taverniers, F.J. Alexander, D.M. Tartakovsky, Noise propagation in hybrid models of nonlinear systems: The Ginzburg-Landau equation, J. Comput. Phys. 262 (2014).

[28] S. Taverniers, D.M. Tartakovsky, A tightly-coupled domain-decomposition approach for highly nonlinear stochastic multiphysics systems, J. Comput. Phys. 330 (2017) 884–901.

[29] I. Yotov, Mixed Finite Element Methods for Flow in Porous Media, Ph.D. thesis, Department of Comp. Appl. Math., Rice University, Houston, TX, 1996.

[30] Y. Yotov, A mixed finite element discretization on non-matching multiblock grids for a generate parabolic equation arising in porous media flow, East-West J. Numer. Math. (1997) 211–230.

[31] M. Peszyńska, M.F. Wheeler, I. Yotov, Mortar upscaling for multiphase flow in porous media, Comput. Geosci. 6 (2002) 73–100.

[32] T. Arbogast, G. Pencheva, M.F. Wheeler, I. Yotov, A multiscale mortar mixed finite element method, Multiscale Model. Simul. 6 (1) (2007) 319–346.

[33] Y. Mehmani, M.T. Balhoff, Bridging from pore to continuum: a hybrid mortar domain decomposition framework for subsurface flow and transport, Multiscale Model. Simul. 12 (2) (2014) 667–693.

[34] Y. Mehmani, M. Oostrom, M.T. Balhoff, A streamline splitting pore-network approach for computationally inexpensive and accurate simulation of species transport in porous media, Water Resour. Res. 50 (3) (2014) 2488–2517.

[35] Y. Tang, A.J. Valocchi, C.J. Werth, A hybrid pore-scale and continuum-scale model for solute diffusion, reaction, and biofilm development in porous media, Water Resour. Res. 51 (3) (2015) 1846–1859.

[36] Y. Mehmami, M.T. Balhoff, Mesoscale and hybrid models of fluid flow and solute transport, Rev. Mineral. Geochem. 80 (2015) 433–459.

[37] P. Jenny, S.H. Lee, H.A. Tchelepi, Adaptive multiscale finite-volume method for multi-phase flow and transport in porous media, Multiscale Model. Simul. 3 (1) (2004) 50–64.

[38] P. Jenny, S.H. Lee, H.A. Tchelepi, Adaptive fully implicit multi-scale finite-volume method for multi-phase flow and transport in heterogeneous porous media, Multiscale Model. Simul. 217 (2) (2006) 627–641.

[39] H. Hajibeygi, P. Jenny, Adaptive iterative multiscale finite volume method, J. Comput. Phys. 230 (3) (2011) 628–643.

[40] P. Tomin, I. Lunati, Hybrid multiscale finite volume method for two-phase flow in porous media, J. Comput. Phys. 250 (2013) 293–307.

[41] T.D. Scheibe, E.M. Murphy, X.Y. Chen, A.K. Rice, K.C. Carroll, B.J. Palmer, A.M. Tartakovsky, I. Battiato, B.D. Wood, An analysis platform for multiscale hydrogeologic modeling with emphasis on hybrid multiscale methods, Transp. Porous Media 53 (1) (2015) 38–56.

[42] I. Battiato, Multiscale models of flow and transport, in: J. Cushman, D.M. Tartakovsky (Eds.), Handbook of Groundwater Engineering, CRC Press, 2016, Ch. 12.

[43] N. Balke, S. Jesse, A.N. Morozovska, E. Eliseev, D.W. Chung, Y. Kim, L. Adamczyk, R.E. García, N. Dudney, S.V. Kalinin, Nanoscale mapping of ion diffusion in a lithium-ion battery cathode, Nat. Nanotechnol. 5 (2010) 749–754.

[44] T.-J. Choi, M.R. Maurya, D.M. Tartakovsky, S. Subramaniam, Stochastic hybrid modeling of intracellular calcium dynamics, J. Chem. Phys. 133 (16) (2010) 165101.

[45] A. Mikelic, V. Devigne, C. Van Duijn, Rigorous upscaling of the reactive flow through a pore, under dominant Peclet and Damkohler numbers, SIAM J. Math. Anal. 38 (4) (2006) 1262–1287.

[46] M. Yousefzadeh, I. Battiato, Second-order IBM reconstruction through normal boundary interpolation, J. Comput. Phys. (2017), submitted for publication.

[47] T. Hayase, J. Humphrey, R. Greif, A consistently formulated quick scheme for fast and stable convergence using finite-volume iterative calculation procedures, J. Comput. Phys. 98 (1) (1992) 108–118.

[48] H.A. Van der Vorst, Bi-CGSTAB: a fast and smoothly converging variant of Bi-CG for the solution of nonsymmetric linear systems, SIAM J. Sci. Stat. Comput. 13 (2) (1992) 631–644.